Optics Letters

Nonlinear post-compression in multi-pass cells in the mid-IR region using bulk materials

D. Carlson,[1,*] M. Tanksalvala,[1] D. Morrill,[1] J. San Roman,[2] E. Conejero Jarque,[2] H. C. Kapteyn,[1] M. M. Murnane,[1] and M. Hemmer[1]

[1]Department of Physics, JILA and STROBE NSF Science & Technology Center, University of Colorado and NIST, Boulder, Colorado, USA
[2]Grupo de Investigaciones en Aplicaciones del Láser y Fotónica, Departamento de Física Aplicada, University of Salamanca, Spain
*Corresponding author: daniel.r.carlson@colorado.edu

Received 27 July 2022; revised 30 August 2022; accepted 7 September 2022; posted 12 September 2022; published 6 October 2022

We numerically investigate the regime of nonlinear pulse compression at mid-IR wavelengths in a multi-pass cell (MPC) containing a dielectric plate. This post-compression setup allows for ionization-free spectral broadening and self-compression while mitigating self-focusing effects. We find that self-compression occurs for a wide range of MPC and pulse parameters and derive scaling rules that enable its optimization. We also reveal the solitonic dynamics of the pulse propagation in the MPC and its limitations and show that spatiotemporal/spectral couplings can be mitigated for appropriately chosen parameters. In addition, we reveal the formation of spectral features akin to quasi-phase matched degenerate four-wave mixing. Finally, we present two case studies of self-compression at 3-μm and 6-μm wavelengths using pulse parameters compatible with driving high-field physics experiments. The simulations presented in this paper set a framework for future experimental work using few-cycle pulses at mid-IR wavelengths.

https://doi.org/10.1364/OL.471458

Nonlinear post-compression methods have enabled routine generation of high-energy few-cycle pulses [1] for a variety of atomic, molecular, and optical science experiments [2], as well as the generation of isolated attosecond pulses. The most ubiquitous nonlinear post-compression implementation consists in coupling intense laser pulses into gas-filled hollow-core fibers [3]. These pulses undergo nonlinear propagation in the waveguide resulting in spectral broadening, mainly due to the interplay between dispersion and self-phase modulation (SPM). This compression technique has led to the generation of 3.8-fs pulses at 800 nm with 6.1 mJ of energy at 1 kHz [4] using meter-scale fibers, 25-fs pulses with 70-mJ energy at 1.03 μm using stretched hollow-core fibers [5], and 75-μJ pulses at 3.1 μm using anti-resonant hollow-core fibers [6]. Filamentation in bulk material in the anomalous dispersion regime has also been demonstrated, yielding self-compressed few-cycle pulses in the mid-IR spectral range [7,8].

Recently, nonlinear compression in multi-pass cells (MPC) has emerged as a powerful and versatile post-compression technique [9–12]. During nonlinear propagation in an MPC, the normally strongly correlated effects of SPM and self-focusing can be mitigated by spreading the nonlinear phase accumulation over many passes, allowing for SPM to occur freely while self-focusing only weakly perturbs the cavity mode. At energies in the few tens of microjoules and near-infrared (NIR) wavelengths, MPCs containing a thin plate of dielectric have been reported to compress pulses with a peak power an order of magnitude larger than the critical power for self-focusing (P_{cr}) without suffering strong nonlinear spatial effects [9,10,13,14,15]. Gas-filled MPCs have enabled the compression of 18-mJ pulses from 1.3-ps to 41-fs duration [16] at a wavelength of 1.03 μm. Self-compression has also been reported in an MPC operated with a dielectric plate using 25-μJ energy pulses at 1.5-μm wavelength [17]. At still higher pulse energies in the 1–10 mJ range, for mid-IR pulses in the 3–4 μm wavelength range, ionization-assisted spatiotemporal localization in gas-filled capillaries has also been observed that can enhance the nonlinear upconversion process of soft x ray high harmonic generation [18,19].

In this Letter, we numerically investigate for the first time the regime of self-compression of mid-IR pulses in MPCs containing a dielectric plate. We investigate the required balance between pulse parameters, MPC design, and material choice to achieve self-compression. We derive general rules to achieve self-compression and show that the propagation in the MPC is solitonic up to a certain peak intensity level. We also investigate the spatiotemporal/spectral couplings that ultimately limit this concept, as well as the stability of the compression with respect to input energy fluctuations. A case study for two realistic laser inputs at 3-μm and 6-μm wavelength is presented that confirms this method as an excellent pathway toward few-cycle mid-IR pulses.

We developed a 4D code that simulates the evolution of the pulse envelope, based on the numerical model proposed in [15], accounting for diffraction, dispersion, and linear absorption, which are evaluated in the Fourier domain, and the self-phase modulation, self-focusing, and self-steepening effects, which are evaluated in the space-time domain. Accounting for all the above phenomena allows our code to accurately describe the dynamics of few-cycle pulses. Nonlinear propagation is simulated via the Fourier split-step method [19]. The linear dispersion and nonlinear contribution of air, the gas filling the MPC, are assumed to be negligible. We tested our code against the experimental results published in [9] and find quantitative agreement. Given the large

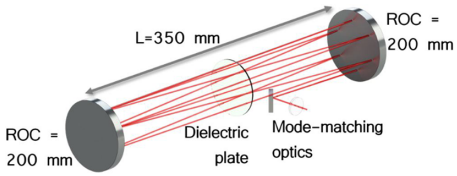

Fig. 1. Layout of the simulated MPC. ROC, radius of curvature.

parameter space to be investigated, we restrict this study to a single cavity design consisting of a symmetrical cavity featuring two mirrors with radii of curvature 200 mm separated by 350 mm (Fig. 1). The plate is always placed at the center of the cavity and is characterized by its Sellmeier equation and nonlinear refractive index. We also limit our study to the wavelengths of 3 μm and 6 μm. The material and thickness of the plate as well as the pulse energy are left as free parameters. The input pulses are temporally Gaussian with a 120-fs duration unless otherwise specified, and the Gaussian input beams are mode-matched to the cavity. The numerical values of the material properties used in the simulations are gathered in Table S1 (Supplement 1).

We first investigate the parameter space defined by the plate thickness ($t = 0.2$–5 mm) and pulse energy ($E = 1$–250 μJ). For a given $\{t, E\}$ pair, we let the pulse make 45 passes through the MPC and record after each pass the pulse duration (full width at half maximum, FWHM) and the pulse cleanliness—defined as the ratio of the energy contained within the FWHM of the temporal intensity profile to the total pulse energy. Note that with this definition, a perfect temporal Gaussian exhibits a cleanliness of 76%. We discard all data for which the spatial intensity profile was altered during propagation—clearly identified when the beam size at the MPC mirrors deviates by 1% from the linear propagation size—and select the pulse with the highest cleanliness to pulse duration ratio as the optimally compressed pulse. We iterate this process to generate the 2D maps shown in Fig. 2.

The four plots shown on Fig. 2 exhibit an area in the upper right corner (high energy, thick plate) in which the data have been discarded because the spatial intensity profile was degraded by self-focusing upon propagation. In the lower right corner (low energy, thick plate), the pulse intensity is too low for the nonlinear spectral phase to balance the group velocity dispersion (GVD) of the material; therefore, the pulse only temporally broadens. In the lower left corner (low energy, thin plate), the pulse is propagating undisturbed experiencing limited linear and

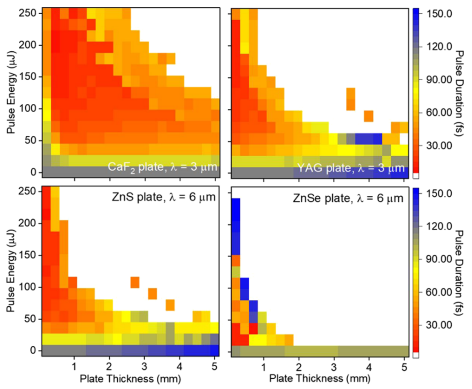

Fig. 2. Mapping of the optimal self-compression regime for pulses at 3-μm wavelength in (top left) CaF_2 and (top right) YAG and at 6-μm wavelength in (bottom left) ZnS and (bottom right) ZnSe.

nonlinear phases. In the upper left corner (high energy, thin plate), self-compression is achieved in some cases. However, the pulses obtained in this regime typically exhibit a broad spectrum that is sub-optimally compressed, owing to the mismatch between GVD and the nonlinear phase. Between these four limiting areas, we observe a region where self-compression occurs. The location of this region in the $\{t, E\}$ diagram depends on the nonlinear and dispersive properties of the plate material. The materials exhibiting the largest nonlinear indices (ZnSe and ZnS) show a limited region where self-compression occurs, confined in the low energy region of the map.

For materials featuring a large GVD at the wavelength of operation, we find that the region to obtain self-compression shifts toward thinner plates—to limit the linear spectral phase accumulation—and higher energy—to balance the linear spectral phase. This is illustrated in Fig. 2 top row, where compression can still be achieved with a 3-mm piece of CaF_2 ($GVD_{3\mu m} = -104$ fs^2/mm) while compression can hardly be achieved in YAG ($GVD_{3\mu m} = -353$ fs^2/mm) for plates thicker than 1 mm. Ultimately, the upper bound for tolerable GVD is related to the onset of ionization in the material—typically in the few TW/cm^2 intensity range for YAG [7]. We also confirm that for materials with a large ratio of third-order dispersion (TOD) to GVD ($\gtrsim$30 fs), the TOD results in post/pre-pulses on the self-compressed temporal intensity profile.

The $\{t, E\}$ maps shown in Fig. 2 provide some insight on the interplay between the material and pulse properties but fail to convey the dynamics of the pulse-shortening pass after pass. To investigate this dynamic, we rely on the soliton number N. We use the definition for N employed in [17], setting $N = \sqrt{L_D/L_{NL}}$, where $L_D = T_0^2/\beta_2$ is the dispersion length and $L_{NL} = \lambda_0/(\pi n_2 I)$ is the nonlinear length, where T_0 is the FWHM duration of the input pulse, β_2 the GVD, λ_0 the central wavelength, n_2 the nonlinear refractive index of the plate material, and I the input peak intensity. For all materials and wavelengths studied, we find that solitonic propagation occurs. For $N < 1$, the pulse only spreads temporally, until reaching $N = 1$, which results in the formation of a first-order soliton (Fig. 3). Increasing the pulse energy to reach $N = 2$ results in the formation of a second-order temporal soliton. For our particular case featuring 120-fs pulses, the soliton duration reached ~50–60 fs for all cases investigated but could not be further shortened. Increasing the pulse energy further ($N \approx 2.59$), the pulse duration breathes over the course of a few tens of passes. In this regime, few-cycle pulses can be obtained if the propagation is interrupted after the appropriate number of passes. For values of $N > 3$, self-compression can be obtained but no soliton is produced: after self-compressing, the pulse breaks up temporally under the effects of higher order dispersion terms. We refrained from further scaling the energy as it could yield spatiotemporal dynamics not captured by our code [20]. Figure 3 illustrates the various regimes of self-compression as a function of N using a 0.5-mm-thick CaF_2 plate at 3 μm. Notice that while the plate thickness does not affect the solitonic propagation in the time domain, it must remain thin enough to avoid falling into the white region of Fig. 2.

Based on the above findings, we perform self-compression simulation for a 100-fs (10 optical cycles) laser system operating at 3 μm and a realistic energy level of 150 μJ. Such systems, operating at 100-kHz repetition rate and above, have been reported [6,21] and find applications in e.g., photoionization studies in the tunneling regime. We also perform a simulation for a 200-fs (10 optical cycles) system operating at 6 μm and 50 μJ of energy

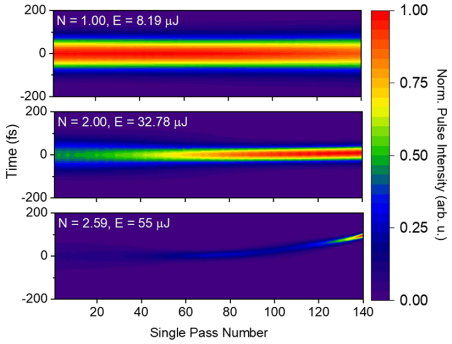

Fig. 3. Evolution of the temporal profile versus number of passes in the cavity for various input energies computed for a 0.5 mm-thick CaF_2 plate at 3 μm wavelength. Transition from (top) absence of compression to (middle) soliton to (bottom) first-order soliton.

to demonstrate the wavelength scalability of our approach. For both simulations, we keep the cavity design shown in Fig. 1 containing a 1-mm-thick plate of CaF_2 and ZnS for the 3-μm and 6-μm case, respectively, yielding a cavity operating in a moderate nonlinear regime ($N = 3.56$ and $N = 4.45$, respectively).

These parameters allow input peak intensities below 1 TW/cm^2 which, in conjunction with the limited thickness of the plate, are expected to prevent filamentation to occur. The pulse peak power is 27 times larger than P_{cr} for CaF_2. We find that after 6.5 round trips, the pulse duration is 19 fs with a pulse cleanliness of 65% [Fig. 4(a)], the FWHM spectral width has increased from 133 nm to 624 nm [Fig. 4(b)], and the perfect Gaussian spatial input intensity profile is unaffected. For the 6-μm wavelength simulation, the input pulse intensity is limited to 0.1 TW/cm^2, 32 times larger than P_{cr} for ZnS. We find that after 8.5 round trips, the input optical pulses are compressed to 42 fs (~2 cycles) with a pulse cleanliness of 69% [Fig. 4(c)] and the spectral width at FWHM is increased from 267 nm to 1117 nm [Fig. 4(d)] while the spatial profile is again left undisturbed and spatiotemporal/spectral couplings are largely mitigated. The bandwidth of the nonlinearly compressed pulses exceeds, by a factor of two, the bandwidths reported from ultrafast mid-IR OPCPAs to date at 5-μm [22] and 7-μm [23] wavelength, thereby

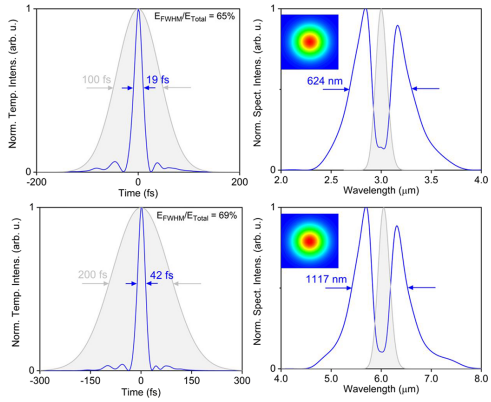

Fig. 4. Input (gray-shaded region) and output (blue line) (top left) temporal and (top right) spectral intensity profiles of a 3-μm wavelength self-compressed pulse along with the output spatial intensity profile in the inset; input (gray-shaded region) and output (blue line) (bottom left) temporal and (bottom right) spectral intensity profiles of a 6-μm wavelength self-compressed along with the output spatial intensity profile in the inset.

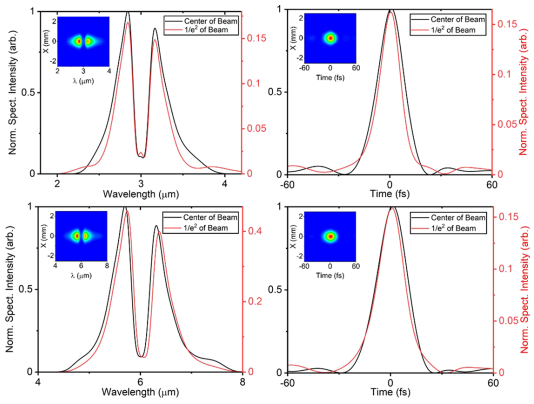

Fig. 5. (left column) Spatiospectral and (right column) spatiotemporal lineouts of (top row) a self-compressed 150-μJ, 3-μm pulse in a 1-mm-thick CaF_2 plate and (bottom row) a self-compressed 50-μJ, 6-μm pulse in a 1-mm-thick ZnS plate. The insets show the corresponding 2D spatiotemporal/spectral profiles

confirming that our approach is a unique pathway to obtain few-cycle pulses in the mid-IR spectral range. Notice that for both simulations, if it was experimentally found that ionization takes place with the parameters chosen here, the cavity design can readily be modified to reduce the peak intensity and still achieve self-compression. The cavity design details are not specific to mid-IR operation—hence beyond the scope of this paper—and have already been investigated in [15].

Pulse compression is typically used to increase the peak intensity of an optical pulse. Such increase should occur with the spatial intensity profile of the beam remaining free from spatiotemporal/spectral couplings upon compression. We performed simulations and retrieved the 2D spatiotemporal/spectral profiles of the self-compressed pulses. To analyze our simulations, these profiles are integrated along the second spatial dimension, and lineouts of the pulse temporal and spectral profiles at the center of the beam and at 1/e^2 of the peak intensity are retrieved. We observe limited couplings (Fig. 5) despite operating orders of magnitude above the critical power. We note that the spatial phase acquired in a single pass is more relevant to destabilizing the cavity than the total phase acquired throughout the propagation. These observations hold true for all materials and wavelengths in Fig. 2.

Our simulations also allow retrieving the full spectral information of the pulses at each pass. We observed that in a regime slightly detuned from optimum self-compression—typically when using plates slightly longer than those providing optimum self-compression all other parameters being kept equal—spectral sidebands appear after a few round trips in the MPC. Similar spectral sidebands have been reported from pulses emerging from gas-filled MPCs—both experimentally [16] and numerically [24]—and those were attributed to quasi-phase matching of degenerate four-wave mixing where the period of the interaction is one trip through the cavity. Our simulations provide the first observation of the formation of similar sidebands in an MPC containing a dielectric plate and a confirmation of the mechanism of their formation. Indeed, we verified that the spectral location of the sidebands satisfies both energy and momentum conservation for degenerate four-wave mixing, $\omega_0 \pm (\omega_0 n_2 I/c|\beta_2|)^{1/2}$ [20], where ω_0 is the central frequency and c is the speed of light in vacuum. This parasitic process appears to remain of low magnitude but is universal in MPCs. We show

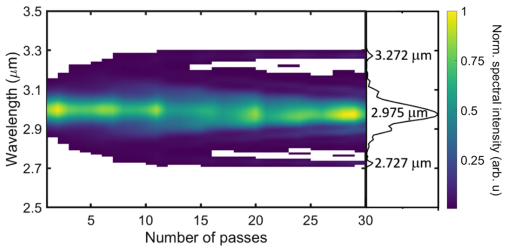

Fig. 6. Spectral evolution during propagation of a 120-fs, 3-μm pulse with 30 μJ in a 2-mm-thick YAG plate. The spectral evolution shows the emergence of spectral side bands that satisfy energy and momentum conservation for a degenerate FWM quasi-phased matched interaction. The plot on the right is a lineout of the spectrum at the 30th pass in the MPC.

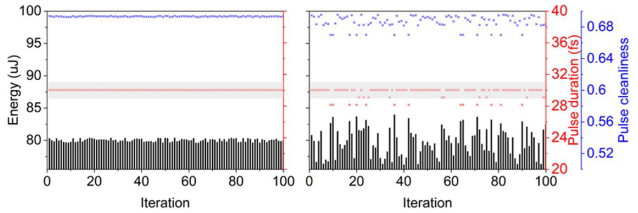

Fig. 7. Pulse duration and pulse cleanliness of a 3.0-μm pulse with 80 μJ of energy after 15 passes through a sapphire MPC with a (left) 1% energy instability and (right) 10% energy instability. The gray-shaded region shows the 1-fs temporal resolution of the code. (For an alternative presentation of the data, please refer to Fig. S1 in Supplement 1)

an example of such side bands formation by propagating 30-μJ energy, 3-μm wavelength pulses in an MPC containing a 2-mm YAG plate (Fig. 6).

Due to the nonlinear nature of the compression process, the effect of energy instability on the output pulse must be considered. This is investigated by introducing either a 1% variance [Fig. 7(a)] or a 10% variance [Fig. 7(b)] on the input pulse energy of a 3-μm pulse with 80 μJ of energy ($N = 3.13$), and calculating the pulse duration and pulse cleanliness after 15 passes through an MPC containing a 0.5-mm-thick sapphire plate. In the 1% case, there is no measurable effect on the pulse duration, and the pulse cleanliness is maintained within 0.5%, which is suitable for most laser applications. In the 10% case, the energy fluctuations begin to affect the balance between SPM and dispersion, as the pulse duration is stable to within 2 fs (7%) and the pulse cleanliness is maintained within 5%. While these simulations provide some insight on the robustness of the MPC approach with respect to energy fluctuations, they do not capture the whole dynamics; for instance, our code does not capture either the Raman effect or the dependence of the carrier envelope phase to input energy. Similarly, our code does not account for atmospheric absorption—a typical issue when operating in the mid-IR—that can induce heating—and hence beam wandering—and additional complex dispersion.

In conclusion, we have shown that self-compression at mid-IR wavelengths in MPCs with a dielectric plate can occur for a broad range of MPC and pulse parameters, yet remains limited to the few tens of μJ energy. We showed that self-compression can be achieved with low spatiotemporal/spectral couplings at 3 μm and 6 μm granted that the plate material is chosen to have an adequate balance between GVD and n_2 in that spectral range. Additionally, we showed that the duration of the self-compressed pulse is hardly affected by pulse energy variations. Future work will consist of incorporating additional nonlinear effects, such as the Raman effect, and verifying these results experimentally. The work presented here provides a roadmap for upcoming filamentation-free self-compression experiments in the mid-IR.

Funding. Air Force Office of Scientific Research (FA9550-16-1-0121); National Nuclear Security Administration (DE-NA0003960); Agencia Estatal de Investigación (PID2019-106910GB-I00).
Acknowledgments. We note that HK is partially employed by KMLabs.
Disclosures. The authors declare no conflicts of interest.
Data availability. The data underlying the results presented in this paper are not publicly available at this time but may be obtained from the authors upon request.
Supplemental document. See Supplement 1 for supporting content.

REFERENCES

1. T. Nagy, P. Simon, and L. Veisz, Adv. Phys. X **6**, 1845795 (2021).
2. B. Wolter, M. G. Pullen, M. Baudisch, M. Sclafani, M. Hemmer, A. Senftleben, C. D. Schröter, J. Ullrich, R. Moshammer, and J. Biegert, Phys. Rev. X **5**, 021034 (2015).
3. M. Nisoli, S. De Silvestri, and O. Svelto, Appl. Phys. Lett. **68**, 2793 (1996).
4. T. Nagy, M. Kretschmar, M. J. J. Vrakking, and A. Rouzée, Opt. Lett. **45**, 3313 (2020).
5. G. Fan, G. Fan, P. A. Carpeggiani, Z. Tao, G. Coccia, R. Safaei, E. Kaksis, A. Pugzlys, F. Légaré, B. E. Schmidt, and A. Baltuška, Opt. Lett. **46**, 896 (2021).
6. U. Elu, M. Baudisch, H. Pires, F. Tani, M. H. Frosz, F. Köttig, A. Ermolov, P. S. J. Russell, and J. Biegert, Optica **4**, 1024 (2017).
7. M. Hemmer, M. Baudisch, A. Thai, A. Couairon, and J. Biegert, Opt. Express **21**, 28095 (2013).
8. V. Shumakova, P. Malevich, S. Alisauskas, A. Voronin, A. M. Zheltikov, D. Faccio, D. Kartashov, A. Baltuska, and A. Pugzlys, Nat. Commun. **7**, 12877 (2016).
9. J. Schulte, T. Sartorius, J. Weitenberg, A. Vernaleken, and P. Russbueldt, Opt. Lett. **41**, 4511 (2016).
10. M. Hanna, F. Guichard, N. Daher, Q. Bournet, X. Délen, and P. Georges, Laser Photonics Rev. **15**, 2100220 (2021).
11. A.-L. Viotti, M. Seidel, E. Escoto, S. Rajhans, W. P. Leemans, I. Hartl, and C. M. Heyl, Optica **9**, 216 (2022).
12. M. G. Hastings, M. G. Hastings, P. Panagiotopoulos, P. Panagiotopoulos, M. Kolesik, M. Kolesik, V. Hasson, V. Hasson, S. Tochitsky, J. v. Moloney, and J. v. Moloney, J. Opt. Soc. Am. B **39**, 266 (2022).
13. N. Daher, F. Guichard, S. W. Jolly, X. Délen, F. Quéré, M. Hanna, and P. Georges, J. Opt. Soc. Am. B **37**, 993 (2020).
14. C. Mei and G. Steinmeyer, Phys. Rev. Res. **3**, 013259 (2021).
15. M. Hanna, X. Délen, L. Lavenu, F. Guichard, Y. Zaouter, F. Druon, and P. Georges, J. Opt. Soc. Am. B **34**, 1340 (2017).
16. M. Kaumanns, V. Pervak, D. Kormin, V. Leshchenko, A. Kessel, M. Ueffing, Y. Chen, and T. Nubbemeyer, Opt. Lett. **43**, 5877 (2018).
17. G. Jargot, N. Daher, L. Lavenu, X. Delen, N. Forget, M. Hanna, and P. Georges, Opt. Lett. **43**, 5643 (2018).
18. A. L. Gaeta, B. Shim, G. Patwardhan, H. C. Kapteyn, M. M. Murnane, T. Popmintchev, and X. Gao, Opt. Lett. **43**, 3112 (2018).
19. G. Agrawal, in *Nonlinear Fiber Optics*, 5th ed. (Elsevier Inc., 2012), pp. 615–617.
20. A. Hofstrand and J. V. Moloney, Phys. Rev. Lett. **124**, 043901 (2020).
21. N. Thiré, R. Maksimenka, B. Kiss, C. Ferchaud, G. Gitzinger, T. Pinoteau, H. Jousselin, S. Jarosch, P. Bizouard, V. di Pietro, E. Cormier, K. Osvay, and N. Forget, Opt. Express **26**, 26907 (2018).
22. L. von Grafenstein, M. Bock, D. Ueberschaer, K. Zawilski, P. Schunemann, U. Griebner, and T. Elsaesser, Opt. Lett. **42**, 3796 (2017).
23. U. Elu, T. Steinle, D. Sánchez, L. Maidment, K. Zawilski, P. Schunemann, U. D. Zeitner, C. Simon-Boisson, and J. Biegert, Opt. Lett. **44**, 3194 (2019).
24. M. Hanna, N. Daher, F. Guichard, X. Délen, and P. Georges, J. Opt. Soc. Am. B **37**, 2982 (2020).